Characterization of human extreme heat exposure using an outdoor thermal manikin

Ankit Joshi,[1,2] Shri H. Viswanathan,[1] Ankush K. Jaiswal,[1,2] Kambiz Sadeghi,[1,21] Lyle Bartels,[1] Rajan M. Jain,[1] Gokul Pathikonda,[1] Jennifer K. Vanos,[2,3] Ariane Middel,[2,4,5] and Konrad Rykaczewski[1,2*]

1. School for Engineering of Matter, Transport and Energy, Arizona State University, Tempe, AZ, USA

2. Julie Ann Wrigley Global Futures Laboratory, Arizona State University, Tempe, AZ, USA

3. School of Sustainability, Arizona State University, Tempe, AZ, USA

4. School for Arts, Media and Engineering, Arizona State University, Tempe, AZ, USA

5. School of Computing and Augmented Intelligence, Arizona State University, Tempe, AZ, USA

*corresponding author email: konradr@asu.edu

Abstract

Extreme heat is a current and growing global health concern. Current heat exposure models include meteorological and human factors that dictate heat stress, comfort, and risk of illness. However, radiation models simplify the human body to a cylinder, while convection ones provide conflicting predictions. To address these issues, we introduce a new method to characterize human exposure to extreme heat with unprecedented detail. We measure heat loads on 35 body surface zones using an outdoor thermal manikin ("ANDI") alongside an ultrasonic anemometer array and integral radiation measurements (IRM). We show that regardless of body orientation, IRM and ANDI agree even under high solar conditions. Further, body parts can be treated as cylinders, even in highly turbulent flow. This geometry-rooted insight yields a whole-body convection correlation that resolves prior conflicts and is valid for diverse indoor and outdoor wind flows. Results will inform decision-making around heat protection, adaptation, and mitigation.

Keywords

Environmental human heat exposure, air turbulence, convection, radiation, thermal manikin, integral radiation measurement

1.Introduction

Extreme heat seriously impacts human health, livability, productivity, and overall well-being (Ebi et al., 2021a, 2021b; Vanos et al., 2023), with age, illness, and poverty aggravating the risk (Jay et al., 2021). As researchers and practitioners seek to contend with increasing heat globally (Cissé et al., 2022; Powis et al., 2023), advanced methods are required to understand the nuances of "heat" exposure—beyond air temperature—that will affect human behavior, technological innovation, infrastructure change, and policy creation (Cissé et al., 2022). These are all critical forms of adaptation that must be targeted to lessen global suffering from heat.

Radiation and convection account for most heat exposure to the human body outdoors (Middel et al., 2016; Parsons, 2019, 2014; Turner et al., 2023) but are more challenging to quantify in urban areas than commonly reported measures of air temperature and humidity (Brown and Gillespie, 1995). The common methods to quantify convective exchange with the human body have been created indoors and have not been validated in real-world outdoor settings, while approaches used to measure radiation exposure (e.g., globe and cylindrical radiation thermometers or integral radiation measurements (IRM)) have not been validated with an accurate, realistic representation of the human body. In particular, the models that intake relevant environmental parameters (e.g., radiative fluxes or wind flow) and output radiative or convective heat fluxes experienced by the human body are either based on simplistic assumptions about the body's shape or provide disagreeing predictions.

The most advanced radiation field measurement method, the IRM, quantifies irradiation in two spectral regions (shortwave and longwave) and six directions (Höppe, 1992; Middel and Krayenhoff, 2019). However, when calculating the radiation absorbed by the body based on the measured twelve fluxes, the IRM assumes that a human body is a single vertical cylinder or box (Brown, 2019; Höppe, 1992; Middel and Krayenhoff, 2019). Exposure to thermal radiation in outdoor settings on human subjects has been studied, but the fluxes were inferred from skin temperature measurements (Blazejczyk et al., 1993), which can be prone to substantial errors (MacRae et al., 2021; Rykaczewski and Dhanote, 2022). Convective heat transfer was also studied with human subjects by directly placing heat flux sensors on the skin (Danielsson, 1996) or measuring the sublimation rate of large naphthalene balls placed on the subject's bodies (Nishi and Gagge, 1970). In both cases, the method could have interfered with airflow (De Dear et al., 1997) and yielded only point values that were not necessarily representative of convection from the local body parts. Instead of working with subjects, more modern efforts to measure convective heat transfer use computational and physical human-shaped thermal manikins (Holmér, 2004; Ichihara, 1997; Ito and Hotta, 2006; Li and Ito, 2012; Psikuta et al., 2017; Xu et al., 2019).

Further, over ten correlations have been developed to predict the forced convective heat transfer coefficient for the human body or its parts based on indoor wind tunnel measurements with thermal manikins or simulations with computational equivalents (Wissler, 2018; Xu et al., 2021). However, for the same wind speed, the prediction of the various correlations can often vary by over 150% (Xu et al., 2021) (see examples in the Supplemental Material—SM). Much of this disagreement stems from not considering or being unable to account for the turbulence characteristics due to wind tunnel limitations. The few recent efforts that account for turbulence intensity (ratio of the standard deviation of the speed fluctuations to its mean value) and, in two cases, length scale (size of large energy-containing eddies) yield several correlations with conflicting coefficients (Ichihara, 1997; Ono et al., 2008; Xu et al., 2021; Yu et al., 2020; Zhou et al., 2022; Zhou and Niu, 2022; Zou et al., 2020). Legacy thermal manikins cannot directly measure radiation, so additional errors might arise from how radiation is estimated and separated from net heat flux to yield the convective flux (De Dear et al., 1997; Fojtlín et al., 2016; Zhou and Niu, 2022). In summary, convective and radiative human heat exposure models use simplistic assumptions or provide conflicting predictions and were not tested in realistic conditions (outdoors and with three-dimensional human body representation). Thus, the multitude of studies applying such models to estimate uncompensable heat outdoors (Coffel et al., 2017; Guzman-Echavarria et al., 2023; Powis et al., 2023; Sherwood and Huber, 2010) or heat balance of outdoors workers or athletes (Dunne et al., 2013; Guzman-Echavarria et al., 2023; Rowlinson and Jia, 2014) may be missing critical aspects to estimate human heat gain and loss in complex settings that people find themselves during heat events.

This paper introduces novel methods to study the impact of extreme heat—and the avenues of heat transfer—on the human body. We leverage a one-of-a-kind thermal manikin—outdoor "ANDI" (see **Fig.1A-C**) alongside a high-end three-level ultrasonic anemometer array and the "MaRTy" biometeorological cart (Middel and Krayenhoff, 2019) (see **Fig.1D**). As legacy manikins, ANDI's shell contains temperature sensors and can be resistively heated. In addition, ANDI’s shell has heat flux sensors and can be water-cooled with built-in liquid channels (see **Fig.1B** and **1C**), thereby enabling convective and direct radiative flux measurements in hot conditions unattainable with prior instrumentation. With a few notable exceptions of legacy manikins being used in mild outdoor settings (e.g., within a car parked outdoors (Danca et al., 2021), wearing protective clothing (Kuklane et al., 2006), or sitting under a shaded lift-up building section (Zhou et al., 2022; Zhou and Niu, 2022)), thermal manikins are operated in pristine climatic chambers while their support systems are in adjacent labs. In contrast, the entire ANDI system, including power and control electronics and water chiller, is mobile and ruggedized to operate in extreme heat and dust (e.g., the electronics are housed in a movable and sealed box with air conditioning, see **Fig.1D**). Here, we deploy this unique suite of instruments for over 20 days in Tempe, Arizona, under extremely hot conditions (air temperatures up to 47°C and irradiation over 1000 W·m^{-2}) to quantify convective and radiative fluxes on ANDI's 35 surface zones. We use the experimental results to examine common assumptions in advanced radiation measurements and provide new physical insight into convection around the human body that sheds light on divergences in prior correlations. While ANDI represents an average male, radiative and convective fluxes (i.e., per surface area) vary slightly with body shape (Rykaczewski et al., 2022a; Viswanathan et al., 2023). The introduced methods are the most advanced way to measure human heat exchange in extreme outdoor environments and provide a novel quantitative understanding that can support better behavioral and policy decisions and optimize technological adaptations.

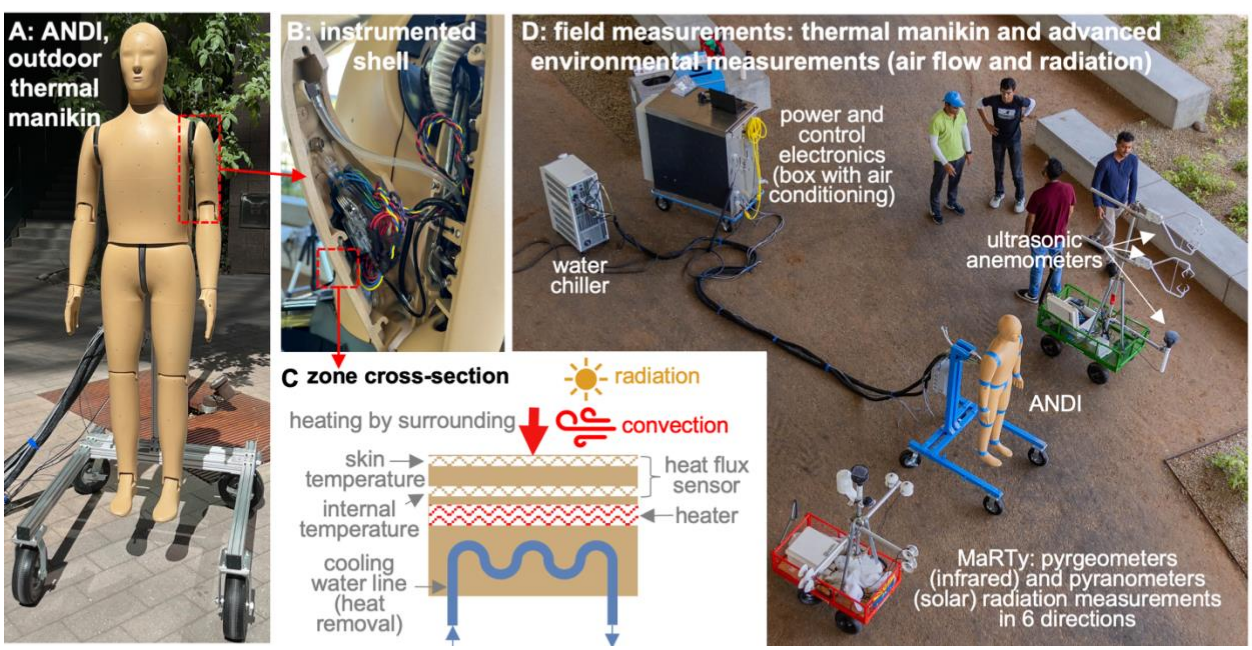

Fig.1 Images of **A.** the outdoor thermal manikin's ("ANDI" – Advanced Newton Dynamic Instrument) exterior and **B.** interior (instrumented shell); **C.** cross-sectional schematic of the manikin's interior with heat flux and temperature sensors, as well as heating and cooling ability that enables radiation and convection measurements in extreme heat conditions, and **D.** "aerial" view of typical outdoor experimental set up showing ANDI and its extreme heat-compatible support systems, the advanced mobile biometeorological station "MaRTy" (Middel and Krayenhoff, 2019), and a three-level 3D ultrasonic anemometer array.

2.Materials and Methods

2.1 Instrumentation

We used a custom outdoor thermal manikin named "Advanced Newton Dynamic Instrument" or ANDI (Thermetrics LLC, Seattle, USA) divided into 35 zones that each contain area-distributed resistive temperature ($\pm$ 0.044 °C accuracy determined by manufacturer calibration) and heat flux sensors and have heating and cooling ability. Each heat flux sensor is custom-made and has an accuracy determined through manufacturer-performed calibration against the heat flux generated with the internal heater. For our thermal manikin, the average absolute measured heat flux deviation from the generated heat flux for the 35 sensors was 3.1% (6.2 $W \cdot m^{-2}$) and at most was 9% (18 $W \cdot m^{-2}$). The manikin represents the 50^{th} percentile of the western male body, with a height of 1.78 meters and a surface area of 1.86 m^2. While based on the base ANDI model, our thermal manikin was customized to be routinely used in extreme heat outdoor conditions. To withstand air temperatures of 50°C and high radiative fluxes (more than 1000 $W \cdot m^{-2}$), the internal part of the shell that includes the cooling channels is made of a higher glass transition polymer than in the regular model. To prevent shading, the manikin is attached to the stand from the back, not through the top of the head as the base manikin model (Joshi et al., 2023). The manikin is suspended 24 cm meters above the ground from a mobile stand covered with non-reflective adhesive (see **Fig.1A** and **1D**). All power electronics, controls, the manikin sweating system (not employed in the current study), and the laptop with control software are housed within the air-conditioned and dust-proof mobile box shown in **Fig.1D**. These systems, along with the water chiller and the manikin, are powered through a mobile gasoline power generator (American Honda Power, Alpharetta, GA; model: EU7000iS). To minimize the impact of the support systems on the manikin measurements, the insulated cooled water inlet and outlet lines and all connecting cables are over 5 m long to avoid any thermal interaction with ANDI. In the constant shell temperature mode, the heat flux sensor, temperature measurements, and the thermofluidic system hardware and controls respond and equilibrate to substantial external condition changes in 6 to 30 s (see the SM), which is about an order of magnitude faster than legacy thermal manikin employed in a study (in sitting position) in transient air flow conditions (Zhou et al., 2022; Zhou and Niu, 2022).

Alongside the thermal manikin, we conducted measurements using the MaRTy biometeorological cart (Middel and Krayenhoff, 2019) and a high-end three-level ultrasonic anemometer array. MaRTy measured shortwave and longwave irradiation fluxes in six directions (four cardinal directions, top, and bottom) using pyranometers and pyrgeometers (both with $\pm$10% accuracy) and the air temperature using HygroClip2 T/RH probe ($\pm$0.1°C accuracy). We used two 3D ultrasonic anemometers (CSAT3B from Campbell Scientific) to measure the outdoor air velocity and turbulence characteristics. A 2D anemometer (Windsonic 1 from Campbell Scientific) measured the wind direction. The anemometers were placed on a mobile cart at a height of 1.8 m, 1.2 m, and 0.6 m from the ground (see **Fig.1D**), while data was collected using CR1000X from Campbell Scientific logger. The logging frequency for 3D anemometers was set to 20 Hz, while 2D anemometer logged data at 1 Hz. The instruments were separated by a distance of 1 to 1.5 m to minimize impact on each other yet to provide measurements of each other (see **Fig.1D**).

2.2 The IRM absorbed radiation and Mean Radiant Temperature (MRT) calculations

We calculated the whole-body absorbed radiation (R_a) by weighting the shortwave (S_j) and longwave (L_j) irradiation fluxes measured using MaRTy with representative spectral band absorptivity values (α_S of 0.7 for shortwave and α_L of 0.97 for longwave radiation (Kántor and Unger, 2011)) and geometrical weights (W_j) corresponding to a single-cylinder human (Höppe, 1992; Middel and Krayenhoff, 2019; Vanos et al., 2021) as follows:

$$R_a = \sum_{j=1}^{6} W_j \left(\alpha_s S_j + \alpha_L L_j\right) \quad (1)$$

The geometrical weight factor for the cardinal directions is 0.22 and 0.06 for the top and down irradiation. The Mean Radiant Temperature (MRT) was calculated from the R_a as:

$$MRT = \sqrt[4]{\frac{R_a}{\alpha_L \sigma}} - 273.15 \quad (2)$$

Where σ is the Stefan-Boltzmann constant equal to 5.67×10^{-8} W·m$^{-2}K^{-4}$. To compare ANDI's measurements against the IRM, we summed the absorbed radiation (units of W) for each of the manikin's zones and divided by the manikin's effective radiation surface area (i.e., area that participates in radiative heat exchange, see the SM).

2.3 Wind flow measurement processing to determine the turbulence characteristics

The outdoor air velocity and turbulence characteristics are complex and non-stationary. We used empirical mode decomposition (EMD) to separate the measured wind speed into time-varying mean and fluctuating components (see the SM). Several studies applied the EMD method in analyzing non-linear and non-stationary air velocity and turbulence characteristics (Jung and Masters, 2013; Ye et al., 2017; Zhou et al., 2022; Zhou and Niu, 2022; Zou et al., 2021, 2020). Savitzky-Golay filtering, which is less cumbersome than EMD analysis, yields closely matching *TI* values (see the SM). The data from our study indicates that the mean air speed is subject to a temporal trend. Therefore, the detrended air speed was considered for calculating the turbulence intensity and length scale, as described in the SM.

The manikin and anemometers were positioned to align with the direction of the wind. Given the highly variable nature of outdoor wind directions, we considered wind within $\pm$45 degrees of the manikin's front exposure as facing the wind for analysis. To filter out any discontinuity in the front direction was also necessary due to the fluctuating nature of outdoor wind directions. To address this, we assumed data continuity if the wind direction deviation was less than 3 s (no more than one data point) from the target wind direction. When narrowed down by the head-on wind direction (at least 30 s steady periods to minimize transient effects), the sub-set of conditions represented the whole range and corresponded to 5,005 individual heat transfer coefficient measurements (143 measurements multiplied by 35 zones).

2.4 Radiation and convection measurements using the thermal manikin

We measured radiation and convection heat exchange at ANDI's skin surface at three locations on the Arizona State University campus in Tempe, Arizona (see location maps in the SM) on clear days from early July to late October 2023. These locations represented unobstructed solar radiation and two types of shade (industrial under a lift-up building and natural shade provided by native Palo Verde trees (Middel et al., 2021)).

The ability to set ANDI's skin temperature (T_{skin_i}) to that of the surrounding air, achieved through sub-ambient water cooling adjusted for each zone with heating, eliminates convection, leading to the measurement of only the net radiative heat flux. To minimize the need for manual adjusting of the skin temperature, we conducted experiments in the afternoons when the air temperature changes only by a fraction of a degree per hour (see example the SM). In all, the air and shell temperature deviation rarely exceeded 0.5 °C. Even with a large heat transfer coefficient of 30 W·m^{-2}°C^{-1}, such a temperature difference would yield a 15 W·m^{-2} that is negligible compared to the radiative fluxes. The thermal manikin measures the net heat flux for (q_{net_i}) in 2 s intervals for the entire body and individual zones (a negative heat flux indicates that the manikin absorbs heat). To calculate the radiative flux absorbed by each zone ($R_{a_{ANDI_i}}$), we added the infrared radiation emitted from that zone into the environment ($R_{e_{ANDI_i}}$) to the measured net heat flux.

$$R_{a_{ANDI_i}} = R_{e_{ANDI_i}} - q_{net_i} = \sigma\, \alpha_L\, F_{ie} T_{skin_i}^4 - q_{net_i} \quad (3)$$

Where i is i^{th} zone of the body and F_{ie} is the zone-environment view factor simulated using an exact 3D manikin model (see the SM). These view factors are needed since other parts of the manikin receive a fraction of the emitted radiation (all isothermal; consequently, there is no net radiation exchange between the body parts).

For quantifying convective heat flux, ANDI's skin temperature was maintained at 5°C below than the air temperature. This temperature difference is smaller than the 12°C specified by the relevant standard for determining thermal insulation of clothing using a heated thermal manikin (ASTM F1291-16, 2004). While such a temperature decrease below ambient was achievable with our system in even hot outdoor conditions, switching between convection and radiation measuring modes required substantial time. Consequently, we settled on the 5°C temperature differential, which owing to the high accuracy of the temperature and heat flux sensors translated into an average and maximum convection measurement accuracy of 6% and 9%, respectively. The net radiative heat flux component ($q_{rad_{ANDI}}$), calculated based on MaRTy-measured

MRT, was subtracted from the net measured heat flux to isolate the convective component of the heat flux ($q_{conv_{ANDI}}$) as:

$$q_{conv_{ANDI}} = q_{net_i} - q_{rad_{ANDI}} = q_{net_i} - \sigma\, \varepsilon\, F_{ie}\left(T_{skin_i}^4 - MRT^4\right) \quad (4)$$

In order to prevent airflow through the manikin's actuated joins, we covered these regions with masking tape (blue tape is visible in **Fig.1D**). Control experiments described in the SM show that the tape had no impact on the measurements.

3. Results

3.1 Radiation

We conducted radiation tests in direct sunlight during clear, sunny, and hot afternoons with stable temperatures (less than 0.5°C per hour change, see SM) ranging from 28 to 43°C, relative humidity of 10 to 20%, wind speed of 0.1 to 5 $m \cdot s^{-1}$, and a solar zenith angle increasing from about 65° to 90°. The maximum directional shortwave and longwave fluxes were observed for the lowest zenith angles (i.e., closer to solar noon) and reached about 800 $W \cdot m^{-2}$ and 575 $W \cdot m^{-2}$, respectively (see the SM). We measured only the net radiative heat flux by setting ANDI's exterior shell temperature to that of air, thereby eliminating convection. To determine the absorbed radiation fluxes for each zone ($R_{a_{ANDI_i}}$), we added longwave emissions from the shell to the net fluxes (see Methods). To quantify the impact of body orientation to the sun, we measured front and side sun exposure on separate days with nearly identical weather conditions (see comparison of the fluxes in the SM). The experiments yield $R_{a_{ANDI_i}}$ for each of the 35 zones (see **Fig.2A**) with fast update period (the heat flux sensor equilibrates rapidly even in response to substantial external changes; see the SM).

The manikin's thermofluidic controls can simultaneously quantify $R_{a_{ANDI_i}}$ across a broad range of fluxes for nearby zones. **Fig.2B** shows that for solar zenith angle of 65° with front sun exposure, $R_{a_{ANDI_i}}$ varies from about 1000 $W \cdot m^{-2}$ on the chest to around 500 $W \cdot m^{-2}$ on the upper back (values for all zones are shown in the SM). The nearly flat zones that are directly facing the sun, as the chest, show the greatest difference when the manikin is turned from front to side, with $R_{a_{ANDI_i}}$ being 350 $W \cdot m^{-2}$ (35%) smaller when the sun is illuminating the manikin's side. In contrast to the flatter zones, the manikin's orientation to the sun has a smaller impact on more convex zones that, in both cases, have large fractions of their area exposed, such as the face (a 150 W·m^{-2} or 18% difference between orientations). The whole-body absorbed radiation flux (i.e., R_a) differs by less than 30 W·m^{-2} between the two orientations, with the side sun exposure values being lower. Next, we compare the R_a measured using ANDI with those obtained using the state-of-the-art MaRTy measurements (i.e., IRM), which cannot provide the radiation fluxes for individual zones.

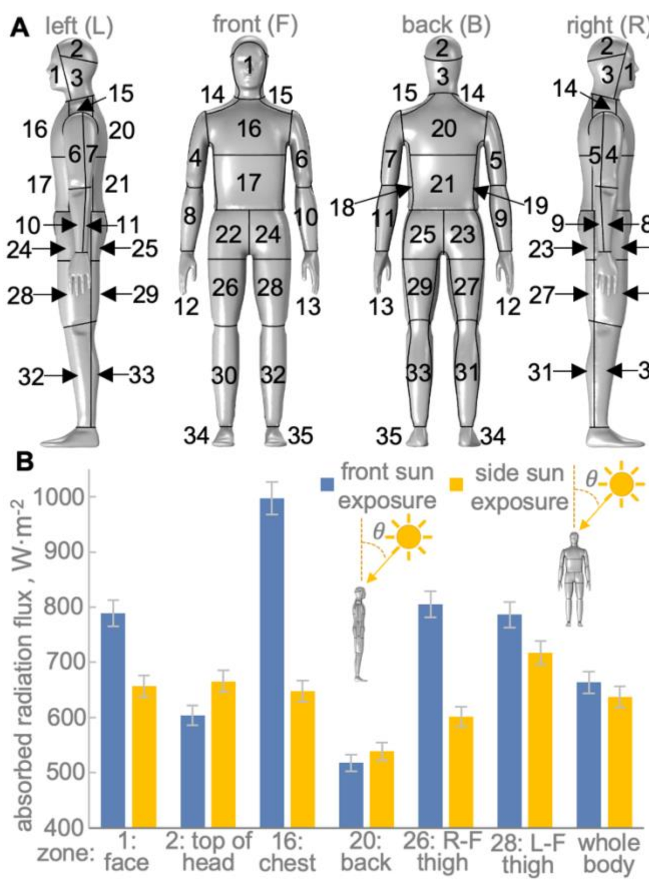

Fig.2 **A.** The layout of ANDI's 35 zones and **B.** Bar graph contrasting absorbed radiative heat flux ($R_{a_{ANDI_i}}$) on select zones under front and side sun exposure with a solar zenith angle of 65° (values for all 35 zones are shown in the SM). The experiments for the two orientations were conducted on separate days but with closely matching conditions and maximum directional shortwave irradiation of about 800 W·m^{-2} and longwave irradiation of about 575 W·m^{-2}.

Fig.3A and **3B** provide a comparison of the R_a measured using ANDI with varied sun-exposure orientations against the IRM (Höppe, 1992; Middel and Krayenhoff, 2019; Vanos et al., 2021). Given that the exterior of the thermal manikin has nearly matching absorptivities (α_S of 0.68 for shortwave and α_L of 0.98 for longwave) to the standard values used for the IRM (see **Eqn. 1** in Methods), a direct comparison of R_a obtained using the two methods is possible. Overall, radiation results show that regardless of body orientation to the sun, the IRM and ANDI measurements agree within instrument uncertainties (mostly below or near 5% and rarely exceeding 10%; **Fig.3C**), even under high solar conditions (e.g., direct beam shortwave radiation, computed from MaRTy fluxes using Holmer's method (Holmer et al., 2015; Rykaczewski et al., 2022b), over 800 $W \cdot m^{-2}$, see the SM), and with lower differences at higher zenith angles. In quantitative terms, the R_a provided by ANDI is at most about 50 to 60 $W \cdot m^{-2}$ lower than the IRM values at zenith angle of 60 to 65°. The decomposition of the IRM signal into the absorbed shortwave and longwave components demonstrates that these differences stem from changes in absorbed shortwave fluxes, given that the longwave fluxes remain constant through the experiments (**Fig.3A** and **3B**). When the R_a is converted to mean radiant temperature (MRT, see **Eqn.2** in Methods), the difference between ANDI and IRM values are below 3 to 4°C for MRT values between 30 and 55°C. Above these MRT values in the most extreme conditions, the difference reaches between about 6°C and 9°C for the front and side sun exposure, respectively. Any differences between ANDI and IRM radiation measurements disappear when the experiments are conducted in a shaded location (see the SM). This observation demonstrates that the IRM method can accurately correct for radiation during manikin-based convection measurements, which we will discuss next.

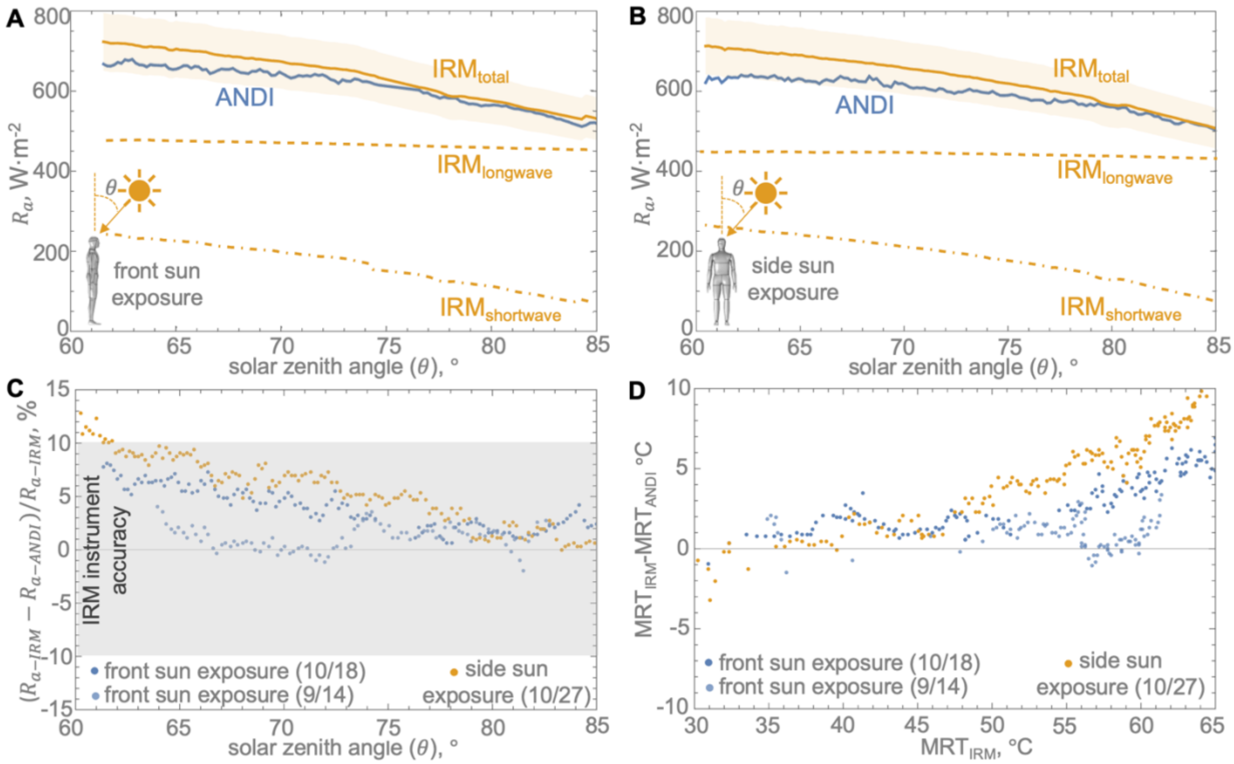

Fig.3 Comparison of whole-body absorbed radiative heat flux (R_a) calculated from ANDI and IRM measurements as a function of solar zenith angle for **A.** front sun exposure and **B.** side sun exposure. The bottom row plots show the difference between the two measurements in terms of **C.** percent and **D.** mean radiant temperature (MRT). We present the fluxes in **A** to **C** as a function of the solar zenith angles to facilitate direct comparison (zenith angle and fluxes variation with time is shown in the SM).

3.2 Convection

We conducted the convection experiments in shaded areas with air temperatures ranging from 39 to 45°C and relative humidity of 10 to 20%, wind speed of 0.7 to 4.5 m·s^{-1} (average of 2.3±0.8 m·s^{-1} (± 1 standard deviation)), turbulence intensity (*TI*) of 0.1 to 46% (average of 15.5±5.5%), and turbulence length scale (L_T) of 0.5 to 15 m (average of 5.3±3.6 m), as shown in **Fig.4A-C**. By setting ANDI's skin temperature below that of air and accounting for radiation through MaRTy measurements, we calculated the convective heat gain from each of the 35 zones (see Methods for details). These measurements are specific to ANDI's zone distribution, which differs from other thermal manikins (De Dear et al., 1997; Li and Ito, 2012; Xu et al., 2019; Zou et al., 2020). To generalize the outcomes beyond ANDI-specific zones, we combined the heat transfer coefficients for individual zones into larger anatomical regions, as shown in

Fig.4D. These regions were defined by grouping ANDI's most relevant zones to match anatomical regions of other manikins for which heat transfer coefficients have been previously reported (De Dear et al., 1997; Li and Ito, 2012; Xu et al., 2019; Zou et al., 2020). The regions might vary to some extent since the manikins are not the same, even representing different genders. The heat transfer coefficients for all the anatomical regions (e.g., calves in **Fig.4E**, see data for rest of the regions in the SM) and whole-body (**Fig.4F**) are strongly correlated to the wind speed, but trends with turbulence characteristics are less evident.

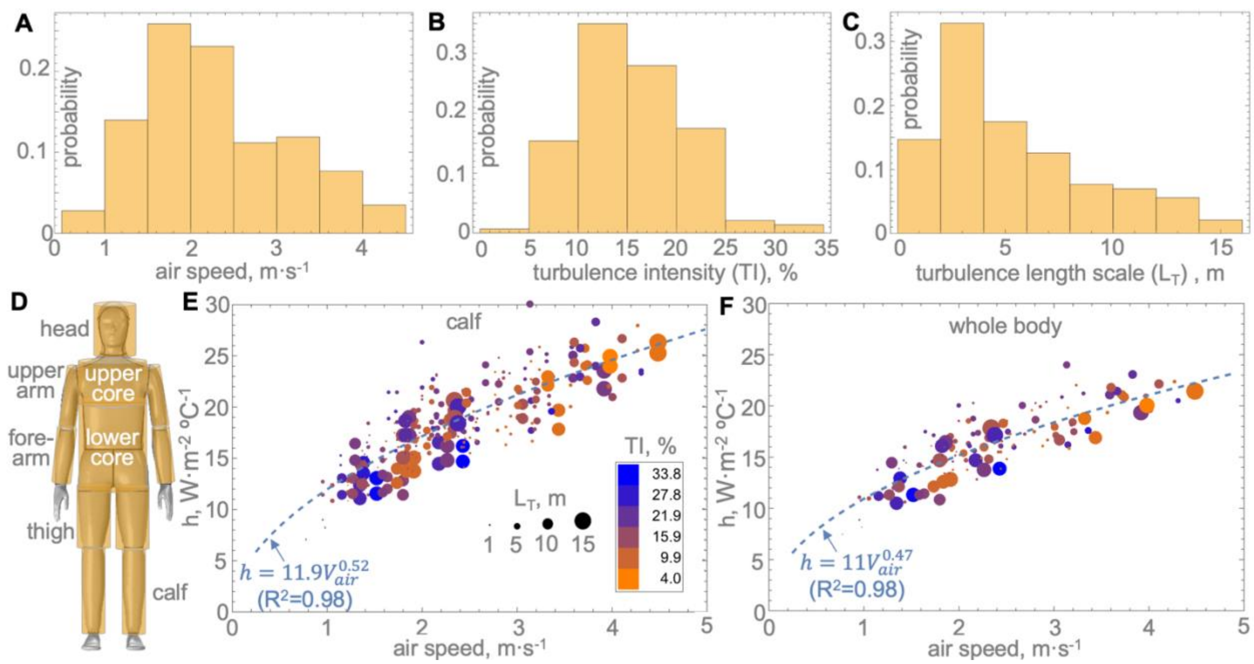

Fig. 4 Histograms of the probability of the **A.** air speed (V_{air}), **B.** turbulence intensity (*TI*), and **C.** turbulence length scale (L_T); **D.** schematic of the anatomical regions grouping multiple ANDI zones, and example heat transfer coefficient (h) measurements for **E.** calf and **F.** whole-body as a function of wind speed. The marker color indicates the *TI,* while its size represents the L_T.

Simulated or measured convection coefficients for the human body are typically presented in terms of empirical correlations that are either a function of wind speed only or also include *TI* and L_T (see **Table 1**). To facilitate comparison of eight prior correlations for whole-body h that are functions of wind speed only (V_{air}), Wissler (Wissler, 2018) calculated modified coefficients, a_m, forcing an exponent of $d = 0.5$ that is expected for a flow around a cylinder (the unmodified exponents vary from 0.49 to 0.60). For our correlation of $h = 11V_{air}^{0.47}$ (see **Fig.4F**), the modified a_m is 10.6, which is near the upper part of the 7.3 to 11 range for prior correlations (see the SM). Our values are towards the upper portion of the range because the turbulence intensity values during the outdoor experiments (average of 15%) were higher than in most wind tunnel experiments. The discrepancies between our outdoor measurements and this simplistic correlation can reach up to 30% (e.g., by 5 W·m^{-2}°C^{-1} from 15 W·m^{-2}°C^{-1} at 2 m·s^{-1}) but can be resolved when turbulence intensity and length scale are considered.

Table 1. Common correlations used to fit convection measurements from the human body are functions of wind speed (V_{air}) only or also include turbulence intensity (*TI*) and length scale (L_T) as variables. The functional form of these equations is based on correlations for cylinders (Hilpert, 1933; Kondjoyan and Daudin, 1995; Sak et al., 2007; Zou et al., 2020) (both non-dimensional and dimensional forms are shown). *Nu* is the Nusselt number, *Re* is the Reynold's number, *Pr* is the Prandtl's number, *h* is the heat transfer coefficient, k_{air} is the thermal conductivity, v_{air} is the kinematic viscosity, *D* the diameter of the cylinder, while *a, b, c, d, n, A, B,* and β are empirical constants.

Form	**Function of V_{air} only** (based on Hilpert (29))	**Function of V_{air}, TI, and L_T** (based on Kondjoyan-Doudin (43) and Sak (44))
non-dimensional (cylinder)	$Nu = cRe^b Pr^{0.33}$	$Nu = 0.63Re^{0.5}(1.07 + 0.015TIRe^{0.5})\left(\frac{L_T}{D}\right)^{-0.09}$
dimensional (cylinder)	$h = cPr^{0.33}\frac{k_{air}}{D}\left(\frac{DV_{air}}{v_{air}}\right)^b$	$h = 0.63\frac{k_{air}}{D}\sqrt{\frac{DV_{air}}{v_{air}}}\left(1.07 + 0.015TI\sqrt{\frac{DV_{air}}{v_{air}}}\right)\left(\frac{L_T}{D}\right)^{-0.09}$
used in empirical correlations	$h = aV_{air}^d$	$h = AV_{air}^n(1 + B \cdot TI \cdot V_{air}^{0.5})(L_T/D)^\beta$

Zou et al. (Zou et al., 2020) and Yu et al.(Yu et al., 2020) proposed a functional form of the heat transfer coefficient correlation, taking into account turbulence characteristics for each body part based on the combination of two engineering correlations for turbulent cross-flow over a cylinder (see Table 1). The terms involving Reynold's number ($Re = DV_{air}/v_{air}$) and *TI* are based on Kondjoyan and Doudin (Kondjoyan and Daudin, 1995) and represent the Nusselt number ($Nu = hD/k_{air}$) for non-turbulent flow and its enhancement with turbulence intensity. The $(L_T/D)^{-0.09}$ is based on Sak et al. (Sak et al., 2007) and accounts for the reduction of the Nu with L_T. Zou et al. (Zou et al., 2020), Yu et al.(Yu et al., 2020), and Zhou et al. (Zhou et al., 2022; Zhou and Niu, 2022) have fitted their simulated or manikin-measured convection measurements for different body regions to the functional form of this equation obtained after substitution of all air properties (see bottom row in Table 1). This approach yields three to four empirical coefficients and exponents per body part and wind direction (i.e., 60 or more empirical coefficients overall). The coefficients for the same scenarios but from different authors vary substantially (see the SM), implying narrow applicability only to the studied range of wind flow characteristics (e.g., L_T on the order of 1 m in wind tunnel experiments). However, such discrepancies can be resolved using a body geometry-rooted analysis approach, as shown below.

To provide better insight into the physics of the convective heat exchange, we fit our heat transfer coefficient data for each anatomical section exposed to head-on flow to the dimensional form of the Kondjoyan-Doudin-Sak equation (see **Table 1**), with the diameter being the only fitting parameter (besides hands and feet; see the rationale in the SM). The resulting "experimental" diameters can be directly compared against geometrical descriptors of the anatomical body parts, such as the hydraulic diameter (D_h is equal to four times the cross-sectional area divided by the perimeter of each "cut" (Bergman et al., 2011)) obtained from analyzing a 3D manikin model (see **Fig.5A** and discussion on head characteristic length in the SM). The bar graph in **Fig.5B** shows that, when considering the variability in both parameters, the diameters derived using the two approaches are in good agreement for nearly all the regions.

Using the diameters obtained from the experiment fitting process, we can non-dimensionalize the heat transfer coefficients into equivalent Nusselt numbers ($Nu_{ANDI} = h_{ANDI}D/k_{air}$) and readily compare all measured values on a single plot against those predicted by substituting measured air flow data into the non-dimensional form of the Kondjoyan-Doudin-Sak equation ($Nu_{K-D}(D, V_{air}, TI, L_T)$). The plot in **Fig.5C** representing all convection measurements for head-on wind direction for all anatomical regions demonstrates that the measured and predicted Nusselt numbers agree well. The scatter of up to 15% is well within the typical spread of engineering convection correlations (often 20% (Bergman et al., 2011)).

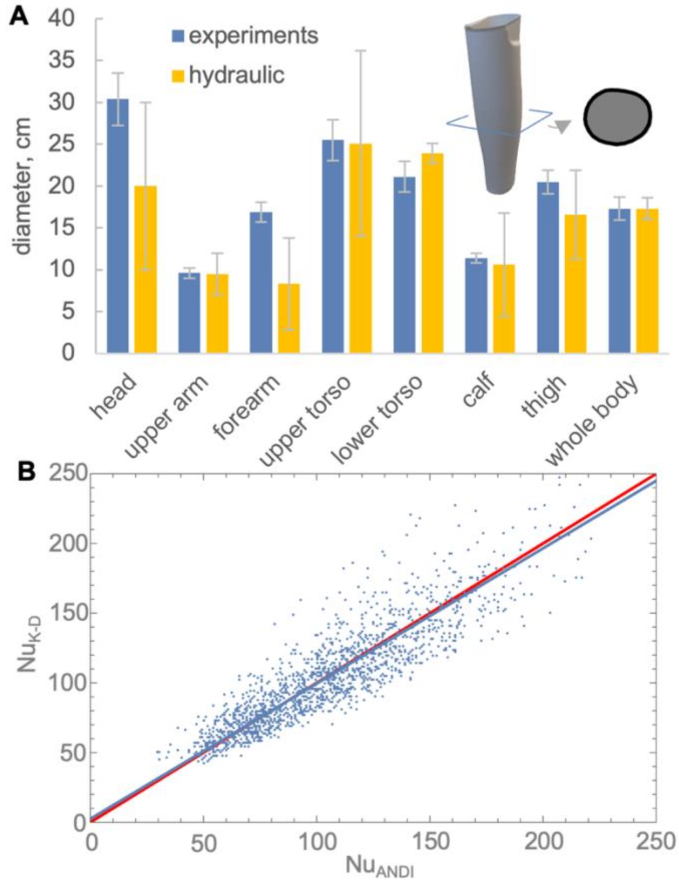

Fig. 5 A. Bar graph comparing equivalent diameters for the anatomical regions shown in Fig.4D derived from the fitting of experimental data and from three-dimensional (3D) model analysis (hydraulic diameter); the inset shows 3D model of ANDI's calf along with an illustrative cross-section used to calculate the equivalent diameter from the cut's area and perimeter, and **B.** comparison of Nusselt numbers employing the determined diameters to compare all convection measurements for the anatomical regions measured using ANDI (Nu_{ANDI}) and against those calculated using measured wind characteristics substituted into the combined Kondjoyan-Daudin-Sak correlation (Nu_{K-D}).

4. Discussion

We introduce novel methods to study the impact of extreme heat—and the avenues of heat transfer—on the human body. We leverage a one-of-a-kind thermal manikin—outdoor "ANDI"—alongside a high-end three-level ultrasonic anemometer array and the "MaRTy" biometeorological cart to perform advanced measurements outdoors. The use of this fully portable measurement system enables convective and direct radiative flux measurements in diverse extremely hot outdoor environments, which has never before been accomplished with a thermal manikin (with exception of few notable studies using thermal manikins in mild outdoor settings (Danca et al., 2021; Kuklane et al., 2006; Zhou et al., 2022; Zhou and Niu, 2022), the instruments are used within climatic chambers). Below, we discuss how radiation and convection measurements conducted using ANDI facilitate validating prior assumptions underlying IRM method and resolving significant discrepancies in convection correlations present in the literature.

4.1 Radiation

The absorbed radiation flux distribution over the body demonstrated here and measured using ANDI has thus far only been available through advanced simulations (Kubaha et al., 2004, 2003; Rees et al., 2008; Rykaczewski et al., 2022b, 2022a). Such detailed information can be used to quantify and improve thermal comfort or heat stress under highly anisotropic radiation (e.g., reflective pavements (Schneider et al., 2023), highly glazed surfaces (Oliveira and Pedrini, 2023; Rees et al., 2008), or hot equipment (Krishnamurthy et al., 2017)) or to optimize the performance of garments made of textiles with engineered spectral properties (Peng and Cui, 2020). However, human thermal radiation exposure is more often assessed in whole-body terms.

Despite the IRM geometrical weights (see **Eqn.1** in Methods) not considering the orientation of the body to the solar radiation, even the largest differences between the radiometer-based and thermal manikin measurements are comparable to the instrument accuracies ($\pm$10% of the value for IRM). As illustrated by separate measurements using ANDI (front exposed to sun) on Sept-14 and Oct-18, shown in **Fig.3C**, a 5% difference can also occur between different experimental repetitions. We note that the difference between the IRM and ANDI experiments is at most 4% in the Sept-14 experiment with the manikin's front sun exposed. Furthermore, the maximum difference observed is unlikely to be larger for lower zenith angles (i.e., closer to noon) because shortwave radiation absorbed by the human body has a relatively small variation at lower zenith angles (i.e., between 8:00-9:00 and 14:00-15:00 in the summertime in Tempe, Arizona (Rykaczewski et al., 2022b; Vanos et al., 2021)), as shown in **Fig.3A,D**. Consequently, the agreement between ANDI and the IRM measurement demonstrates that the latter provides a good measure of the R_a for a standing human, regardless of their orientation to the sun. This observation is essential as the IRM is often used as the "gold standard" for comparison of whole-body absorbed radiation flux measured using a variety of lower cost and widely utilized instruments (e.g., globe, cylindrical, and ping-pong ball radiation thermometers (Guo et al., 2020; Thorsson et al., 2007; Vanos et al., 2021)).

4.2 Convection

Fitting our data yields an equivalent diameter for the whole body of 17.3 cm, which when substituted along with turbulence characteristics into the combination of two engineering correlations for a cylinder in turbulent cross-flow (the dimensional form of the Kondjoyan-Doudin-Sak equation) provides matching predictions to most convection correlations that otherwise provide conflicting outcomes. We note that this equivalent diameter can also be obtained using an area-weighted average of diameters for the anatomical regions. The plot in **Fig.6A** shows that our heat transfer coefficient predictions employing this diameter closely match the correlations of De Dear et al. (19) and Oguro et al. (51). These correlations are only a function of wind speed but were measured with TI of 4% to 8% and L_T of about 1 m (generated using a large vertical cylinder in the wind tunnel). When TI is increased to the range that pedestrians experience outdoors (about 20%), our predictions also match well with those of Yu et al.(Yu et al., 2020) and, below 3 $m \cdot s^{-1}$, with Zhou et al.(Zhou et al., 2022) (which is the upper wind speed limit of the latter correlation). Similarly, when L_T is adjusted to likely low values (order of 5 to 10 cm) in the works of Xu et al.(Xu et al., 2021) and Ono et al.(Ono et al., 2008), our correlations are in good agreement (see **Fig.6B** and **6C**).

From the correlations for which TI and L_T are included or can be estimated, our correlation only differs substantially from the simulation-based Zou et al.(Zou et al., 2020) correlation (see the SM). The latter correlation predicts values at least 30% higher than many other reported values (Zou et al., 2020) but roughly agree with those reported by Ichihara et al.(Ichihara, 1997) (which has insufficient information to deduct TI and L_T values). The discrepancy between our correlation and that of Zou et al. (Zou et al., 2020) stems primarily from the higher weighting of TI ($B = 2$ vs. equivalent 1.53 for our work) and lower exponent on L_T (β =-0.05 vs. -0.09 for our work). It might be the result of varied methods, or the relatively narrow L_T range (2.5 to 6 m) used in their simulations. Other sources of disagreement between the convective correlations might be how radiative heat exchange is estimated for different body parts and subtracted from measured heat flux to provide the convection value. Legacy thermal manikins used in past studies cannot directly measure radiation, so it was either minimized by adding low emissivity foil coatings (De Dear et al., 1997; Fojtlín et al., 2016) or calculated using local view factors along with MRT (Zhou et al., 2022; Zhou and Niu, 2022). The outcomes of the former method might have been skewed by air trapped under the foil, while those of the latter method might have been impacted by the generic nature of the view factors (not manikin and pose specific) and error-prone globe meters used to measure the MRT (Vanos et al., 2021; Zhou et al., 2022; Zhou and Niu, 2022). Our convection measurements do not suffer such shortcomings since we rely on IRM measurements validated against ANDI's equivalents and use view factors specific to our manikin and its posture (see Methods and SM). We also note that changes in air properties with temperatures in the 20 to 50°C range have a negligible net impact on the heat transfer coefficient (Viswanathan et al., 2023).

Overall, our geometry-rooted approach demonstrates that different body parts are well-approximated by cylinders even in turbulent flow and can also match most of the prior correlations for whole-body heat transfer coefficients. We note that the diameter-based approach works well when ANDI faces the wind, as body parts have a relatively small impact on the flow around each other and behave similarly to isolated cylinders. Such interactions could be substantially higher with side-on flow. Although engineering heat transfer correlations for flow over sequential tubes in a bank exist, they do not consider the flow's incoming turbulence (Bergman et al., 2011). Consequently, an approach based on correlations with multiple fitting parameters is more practical for such cases.

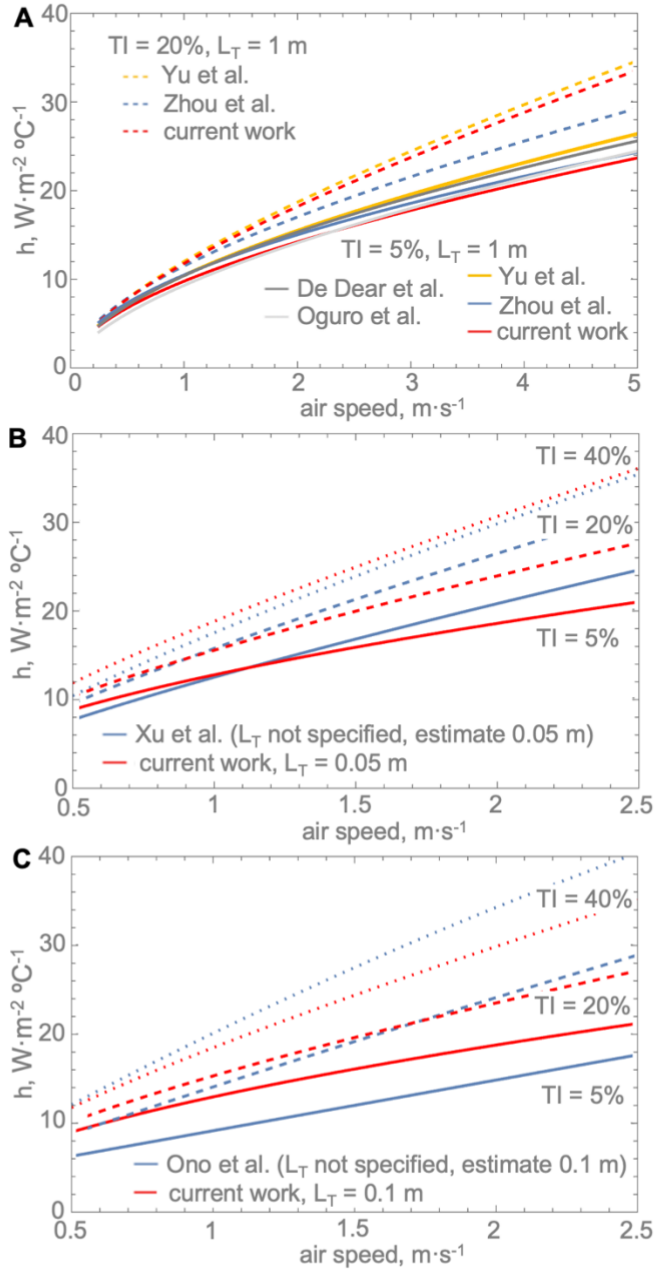

Fig. 6 A-C: Comparison of current whole-body heat transfer coefficient (h) correlations against those in the literature for varied turbulence intensity (TI) and length scale (L_T) values (see the SM for tabulated correlations).

4.3 Limitations

There are several limitations, areas for improvement, and opportunities for future studies beyond the current work. Thus far, we only conducted measurements with the manikin in a static standing position, emphasizing front wind exposure. Both the radiative (Fanger, 1972; Park and Tuller, 2011a, 2011b) and the convective (De Dear et al., 1997; Gaspar et al., 2006; Vogt et al., 1983a; Xu et al., 2021) heat exposure are impacted by changes in posture (e.g., sitting vs. standing), the subject's motion, and the presence of clothing. In contrast to the IRM, the thermal manikin cannot provide radiation measurements for spectral regions that might clarify how to engineer radiative properties of the built environment (Schneider et al., 2023) or clothing (Peng and Cui, 2020). In turn, for convection measurements, we employed the isotropic radiation assumption that could impact some local convective fluxes. We note that we did conduct pilot experiments switching between radiation (i.e., ANDI at air temperature) and convection (i.e., ANDI cooler than the surrounding) measurement, but we found that the time required for this process was too long to do continuously. In other words, we found better outcomes by using the MaRTy cart to quantify the radiation at a fast rate, which captured small, but significant fluctuations in the irradiation. This point leads to the primary limitation of our approach: the chaotic nature of the outdoor environments. The chaotic features are most pronounced for wind flow, which can fluctuate substantially even within the 30 s periods we focus on. In extremely hot desert conditions, short bursts of air can also be accompanied by locally higher air temperature, which on rare occasions can overwhelm the thermofluidic systems on a zone or two (as exemplified by occasional near zero heat transfer coefficients for 1/35 zones in a given time period). Consequently, we can inherently expect outdoor measurements to produce a higher scatter in convective measurements than equivalents in a wind tunnel. In addition, we note that clothing ventilation and pumping effects induced by motion can substantially alter air flow and heat transfer around the body (Bouskill et al., 2002; Kang et al., 2020; Vogt et al., 1983b), therefore will be included in future experimentation.

5. Conclusions

The introduced suite of instruments–including the outdoor thermal manikin ANDI, the MaRTy biometeorological cart, and the ultrasonic anemometer array–is the most advanced way to characterize the dominant components of the thermal load—convection and radiation—on humans exposed to extreme heat. The thermal manikin was custom-designed and successfully deployed for routine outdoor measurements of the radiative and convective heat fluxes on 35 human body surface areas in extremely hot conditions.

The simultaneous ANDI and MaRTy radiative measurements allowed us to test the common assumption of cylindrical body shape used in the IRM method. In particular, we showed that even under high solar conditions, IRM and ANDI agree with radiative measurements within instrument uncertainties regardless of body orientation. Any disagreement in the measures of radiation absorbed by the whole-body disappears when experiments are conducted in shaded conditions. While the overall difference in the R_a for the entire body remains negligible under different body orientations to the sun, it is noteworthy that there are substantial deviations observed in local body parts. The high spatial resolution data from ANDI allows us to delve deeper into the radiation fluxes at localized body parts. Considering the availability of this detailed data, shedding light on these localized aspects can significantly contribute to a more comprehensive and nuanced understanding in practical applications.

We used ANDI's convective measurements to show that anatomical body regions can be treated as cylinders even in highly turbulent flow. This geometry-rooted analysis of the convective measurements yields an appropriate equivalent diameter for the human body (17.3 cm). When this proper length scale for the body and turbulence variables are substituted into traditional engineering correlation for a cylinder in cross-flow, the results match predictions of most convection correlations that otherwise provide conflicting outcomes. Consequently, the introduced physics-based correlation is universally applicable across a wide range of wind speeds, TI, and L_T, covering indoor and outdoor settings, and based on our prior work, to diverse human body shapes (Viswanathan et al., 2023). These results provide more advanced estimates of human heat exchange in extreme outdoor environments, providing a novel quantitative understanding of how a hot environment heats humans.

The ability to predict heat exchange experienced by ANDI based on microclimatic measurements (i.e., radiometers and anemometers) also lays the foundation for future work conducting outdoor "adaptive" mode experiments. In this mode, the thermal manikin is controlled by a thermoregulation model and has physiologically based responses to the environmental and metabolic heat loads (e.g., sweats more when hot (Blood and Burke, 2010; Burke et al., 2010, 2009; Joshi et al., 2023; Psikuta et al., 2017)). Therefore, using the introduced suite of instruments, we can quantify the dynamics of physiological responses (e.g., core and skin temperatures; sweat rate) to specific combinations of hot microclimates (quantified using MaRTy and anemometers) with human factors such as metabolic rates (adjusted for with ANDI) and clothing. This is a unique method to test various scenarios, including experiments in which the thermal exposure and duration become dangerous to humans and, therefore, cannot be conducted. Overall, current results and future adaptive experimentation in various outdoor settings contribute to developing strategies to adapt urban planning, clothing design, and outdoor activity to changing climate conditions, thus supporting informed decision-making around heat protection, adaptation, and mitigation.

Acknowledgments

This research was supported by the National Science Foundation Leading Engineering for America's Prosperity, Health, and Infrastructure (LEAP HI) #2152468 award, while the thermal manikin was funded by a National Science Foundation Major Research Instrumentation grant #2117917. We also thank Rick Burke from Thermetrics LLC for his technical support and Samantha Chow Arizona State University for permission to use "aerial view" photograph of the thermal manikin setup in Fig.1D. The authors gratefully acknowledge the use of spectroscopy equipment within the Eyring Center for Solid State Science at Arizona State University.

Author Contributions

Conceptualization: KR, JKV, AM

Methodology: KR, AM, AJ, LB, SHV, GP

Investigation: AJ, SHV, AKJ, LB, RMJ, KS, KR

Visualization: KR, AJ, SHV, LB

Supervision: KR, JKV, AM

Writing—original draft: AJ, KR, JKV, AM

Writing—reviewing and editing: KR, AJ, JKV, AM, LB, SHV, GP, RMJ, KS

Competing Interests: Authors declare that they have no competing interests.

Data Availability

The heat transfer coefficients for all zones and processing Matlab codes will be available on https://dataverse.asu.edu/ upon publication.

Supplementary Materials

Is available and covers details of the measurements and further comparisons of outcomes against correlations in the literature.

References

ASTM F1291-16, 2004. Standard Test Method for Measuring the Thermal Insulation of Clothing Using a Heated Manikin. American Society for Testing and Materials Book of Standards .

Bergman, T.L., Lavine, A.S., Incropera, F.P., Dewitt, D.P., 2011. Fundamentals of heat and mass transfer. John Wiley & Sons, Inc, New York.

Blazejczyk, K., Nilsson, H., Holmér, I., 1993. Solar heat load on man. Int J Biometeorol 37, 125–132.

Blood, K., Burke, R., 2010. Further validation of the model-controlled Newton thermal manikin against historical human studies, in: 8th International Meeting for Thermal Manikin and Modeling (8I3M), Victoria, Canada.

Bouskill, L.M., Havenith, G., Kuklane, K., Parsons, K.C., Withey, W.R., 2002. Relationship between clothing ventilation and thermal insulation. AIHA journal 63, 262–268.

Brown, R.D., 2019. Correcting the Error in Measuring Radiation Received by a Person: Introducing Cylindrical Radiometers. Sensors 19, 5085.

Brown, R.D., Gillespie, T.J., 1995. Microclimate Landscape Design. John Wiley & Sons, Inc.

Burke, R., Blood, K., Deaton, A.S., Barker, R., 2010. Application of model-controlled manikin to predict human physiological response in firefighter turnout gear, in: 8th International Meeting for Thermal Manikin and Modeling (8I3M), Victoria, Canada.

Burke, R., Curran, A., Hepokoski, M., 2009. Integrating an active physiological and comfort model to the Newton sweating thermal manikin, in: 13th International Conference on Environmental Ergonomics. Boston, USA.

Cissé, G., McLeman, R., Adams, H., Aldunce, P., Bowen, K., Campbell-Lendrum, D., Clayton, S., Ebi, K.L., Hess, J., Huang, C., 2022. 2022: health, wellbeing, and the changing structure of communities.

Coffel, E.D., Horton, R.M., De Sherbinin, A., 2017. Temperature and humidity based projections of a rapid rise in global heat stress exposure during the 21st century. Environmental Research Letters 13, 014001.

Danca, P.A., Nastase, I., Croitoru, C., Bode, F., Sandu, M., 2021. Thermal comfort evaluation inside a car parked under sun and shadow using a thermal manikin, in: IOP Conference Series: Earth and Environmental Science. IOP Publishing, p. 012064.

Danielsson, U., 1996. Convection coefficients in clothing air layers.

De Dear, R.J., Arens, E., Hui, Z., Oguro, M., 1997. Convective and radiative heat transfer coefficients for individual human body segments. Int J Biometeorol 40, 141–156.

Dunne, J.P., Stouffer, R.J., John, J.G., 2013. Reductions in labour capacity from heat stress under climate warming. Nat Clim Chang 3, 563.

Ebi, K.L., Capon, A., Berry, P., Broderick, C., de Dear, R., Havenith, G., Honda, Y., Kovats, R.S., Ma, W., Malik, A., 2021a. Hot weather and heat extremes: health risks. The lancet 398, 698–708.

Ebi, K.L., Vanos, J., Baldwin, J.W., Bell, J.E., Hondula, D.M., Errett, N.A., Hayes, K., Reid, C.E., Saha, S., Spector, J., 2021b. Extreme weather and climate change: population health and health system implications. Annu Rev Public Health 42, 293.

Fanger, P.O., 1972. Thermal Comfort. McGraw-Hill Book Company, New York.

Fojtlín, M., Fišer, J., Jícha, M., 2016. Determination of convective and radiative heat transfer coefficients using 34-zones thermal manikin: Uncertainty and reproducibility evaluation. Exp Therm Fluid Sci 77, 257–264.

Gaspar, A.R., Oliveira, A. V, Quintela, D.A., 2006. Effects of walking and air velocity on convective heat transfer from a nude manikin, in: Winsdor Conference: Comfort and Energy Use in Buildings: Getting Them Right–International Conference, Windsor Great Park, UK. pp. 27–30.

Guo, H., Aviv, D., Loyola, M., Teitelbaum, E., Houchois, N., Meggers, F., 2020. On the understanding of the mean radiant temperature within both the indoor and outdoor environment, a critical review. Renewable and Sustainable Energy Reviews 117, 109207.

Guzman-Echavarria, G., Middel, A., Vanos, J., 2023. Beyond heat exposure—new methods to quantify and link personal heat exposure, stress, and strain in diverse populations and climates: The journal temperature toolbox. Temperature 1–21.

Hilpert, R., 1933. Heat transfer from cylinders. Forsch. Geb. Ingenieurwes 4, 215.

Holmer, B., Lindberg, F., Rayner, D., Thorsson, S., 2015. How to transform the standing man from a box to a cylinder–a modified methodology to calculate mean radiant temperature in field studies and models, in: Proceedings of the 9th International Conference on Urban Climate (ICUC9), Toulouse, France. pp. 20–24.

Holmér, I., 2004. Thermal manikin history and applications. Eur J Appl Physiol 92, 614–618.

Höppe, P., 1992. Ein neues Verfahren zur Bestimmung der mittleren Strahlungstemperatur im Freien. Wetter und Leben 44, 147–151.

Ichihara, M., 1997. Measurement of Convective and Radiative Hear Transfer Coefficients for the Standing and Sitting Human Body Using a Thermal Manikin. J. Archit. Plann. Environ. Eng., AIJ 501, 45–51.

Ito, K., Hotta, T., 2006. Development of Virtual Manikins and its grid library for CFD Analysis. 空気調和・衛生工学会論文集 27–33.

Jay, O., Capon, A., Berry, P., Broderick, C., de Dear, R., Havenith, G., Honda, Y., Kovats, R.S., Ma, W., Malik, A., 2021. Reducing the health effects of hot weather and heat extremes: from personal cooling strategies to green cities. The Lancet 398, 709–724.

Joshi, A., Bartels, L., Viswanathan, S.H., Martinez, D.M., Sadeghi, K., Jaiswal, A.K., Collins, D., Rykaczewski, K., 2023. Evaluation of thermal properties and thermoregulatory impacts of lower back exosuit using thermal manikin. Int J Ind Ergon 98, 103517.

Jung, S., Masters, F.J., 2013. Characterization of open and suburban boundary layer wind turbulence in 2008 Hurricane Ike. Wind and structures 17, 135–162.

Kang, Z., Shou, D., Fan, J., 2020. Numerical modeling of body heat dissipation through static and dynamic clothing air gaps. Int J Heat Mass Transf 157, 119833. https://doi.org/https://doi.org/10.1016/j.ijheatmasstransfer.2020.119833

Kántor, N., Unger, J., 2011. The most problematic variable in the course of human-biometeorological comfort assessment—the mean radiant temperature. Central European Journal of Geosciences 3, 90–100.

Kondjoyan, A., Daudin, J.-D., 1995. Effects of free stream turbulence intensity on heat and mass transfers at the surface of a circular cylinder and an elliptical cylinder, axis ratio 4. Int J Heat Mass Transf 38, 1735–1749.

Krishnamurthy, M., Ramalingam, P., Perumal, K., Kamalakannan, L.P., Chinnadurai, J., Shanmugam, R., Srinivasan, K., Venugopal, V., 2017. Occupational heat stress impacts on health and productivity in a steel industry in Southern India. Saf Health Work 8, 99–104.

Kubaha, K., Fiala, D., Lomas, K.J., 2003. Predicting human geometry-related factors for detailed radiation analysis in indoor spaces.

Kubaha, K., Fiala, D., Toftum, J., Taki, A.H., 2004. Human projected area factors for detailed direct and diffuse solar radiation analysis. Int J Biometeorol 49, 113–129.

Kuklane, K., Gao, C., Holmér, I., 2006. Effects of natural solar radiation on manikin heat exchange, in: 3rd European Conference on Protective Clothing and NOKOBETEF 8. Protective Clothing-towards Balanced Protection. Central Institute for Labour Protection, Warszawa, Poland.

Li, C., Ito, K., 2012. Numerical analysis of convective heat and mass transfer around human body under strong wind. International Journal of High-Rise Buildings 1, 107–116.

MacRae, B.A., Spengler, C.M., Psikuta, A., Rossi, R.M., Annaheim, S., 2021. A thermal skin model for comparing contact skin temperature sensors and assessing measurement errors. Sensors 21, 4906.

Middel, A., Alkhaled, S., Schneider, F., Hagen, B., Coseo, P., 2021. 50 Grades of Shade. Bull Am Meteorol Soc 1–35.

Middel, A., Krayenhoff, E.S., 2019. Micrometeorological determinants of pedestrian thermal exposure during record-breaking heat in Tempe, Arizona: Introducing the MaRTy observational platform. Science of the total environment 687, 137–151.

Middel, A., Selover, N., Hagen, B., Chhetri, N., 2016. Impact of shade on outdoor thermal comfort—a seasonal field study in Tempe, Arizona. Int J Biometeorol 60, 1849–1861.

Nishi, Y., Gagge, A.P., 1970. Direct evaluation of convective heat transfer coefficient by naphthalene sublimation. J Appl Physiol 29, 830–838.

Oliveira, A., Pedrini, A., 2023. Thermal performance of highly glazed office buildings in the tropics: Contradicting architectś expectations. Energy Build 296, 113344.

Ono, T., Murakami, S., Ooka, R., Omori, T., 2008. Numerical and experimental study on convective heat transfer of the human body in the outdoor environment. Journal of Wind Engineering and Industrial Aerodynamics 96, 1719–1732.

Park, S., Tuller, S.E., 2011a. Human body area factors for radiation exchange analysis: standing and walking postures. Int J Biometeorol 55, 695–709.

Park, S., Tuller, S.E., 2011b. Comparison of human radiation exchange models in outdoor areas. Theor Appl Climatol 105, 357–370.

Parsons, K., 2019. Human heat stress. CRC Press.

Parsons, K., 2014. Human thermal environments: the effects of hot, moderate, and cold environments on human health, comfort, and performance. CRC press.

Peng, Y., Cui, Y., 2020. Advanced textiles for personal thermal management and energy. Joule 4, 724–742.

Powis, C.M., Byrne, D., Zobel, Z., Gassert, K.N., Lute, A.C., Schwalm, C.R., 2023. Observational and model evidence together support wide-spread exposure to noncompensable heat under continued global warming. Sci Adv 9, eadg9297.

Psikuta, A., Allegrini, J., Koelblen, B., Bogdan, A., Annaheim, S., Martínez, N., Derome, D., Carmeliet, J., Rossi, R.M., 2017. Thermal manikins controlled by human thermoregulation models for energy efficiency and thermal comfort research–A review. Renewable and Sustainable Energy Reviews 78, 1315–1330.

Rees, S.J., Lomas, K.J., Fiala, D., 2008. Predicting local thermal discomfort adjacent to glazing.

Rowlinson, S., Jia, Y.A., 2014. Application of the predicted heat strain model in development of localized, threshold-based heat stress management guidelines for the construction industry. Annals of occupational hygiene 58, 326–339.

Rykaczewski, K., Bartels, L., Martinez, D.M., Viswanathan, S.H., 2022a. Human body radiation area factors for diverse adult population. Int J Biometeorol 66, 2357–2367.

Rykaczewski, K., Dhanote, T., 2022. Analysis of thermocouple-based finger contact temperature measurements. J Therm Biol 103293.

Rykaczewski, K., Vanos, J.K., Middel, A., 2022b. Anisotropic radiation source models for computational thermal manikin simulations based on common radiation field measurements. Build Environ 208, 108636.

Sak, C., Liu, R., Ting, D.-K., Rankin, G.W., 2007. The role of turbulence length scale and turbulence intensity on forced convection from a heated horizontal circular cylinder. Exp Therm Fluid Sci 31, 279–289.

Schneider, F.A., Ortiz, J.C., Vanos, J.K., Sailor, D.J., Middel, A., 2023. Evidence-based guidance on reflective pavement for urban heat mitigation in Arizona. Nat Commun 14, 1467.

Sherwood, S.C., Huber, M., 2010. An adaptability limit to climate change due to heat stress. Proceedings of the National Academy of Sciences 107, 9552–9555.

Thorsson, S., Lindberg, F., Eliasson, I., Holmer, B., 2007. Different methods for estimating the mean radiant temperature in an outdoor urban setting. Int J Climatol 27, 1983–1993.

Turner, V.K., Middel, A., Vanos, J.K., 2023. Shade is an essential solution for hotter cities. Nature 619, 694–697.

Vanos, J., Guzman-Echavarria, G., Baldwin, J.W., Bongers, C., Ebi, K.L., Jay, O., 2023. A physiological approach for assessing human survivability and liveability to heat in a changing climate. Nat Commun 14, 7653. https://doi.org/10.1038/s41467-023-43121-5

Vanos, J.K., Rykaczewski, K., Middel, A., Vecellio, D.J., Brown, R.D., Gillespie, T.J., 2021. Improved methods for estimating mean radiant temperature in hot and sunny outdoor settings. Int J Biometeorol 65, 967–983.

Viswanathan, S.H., Martinez, D.M., Bartels, L., Guddanti, S.S., Rykaczewski, K., 2023. Impact of human body shape on forced convection heat transfer. Int J Biometeorol 1–9.

Vogt, J.J., Meyer, J.P., Candas, V., Libert, J.P., Sagot, J.C., 1983a. Pumping effects on thermal insulation of clothing worn by human subjects. Ergonomics 26, 963–974.

Vogt, J.J., Meyer, J.P., Candas, V., Libert, J.P., Sagot, J.C., 1983b. Pumping effects on thermal insulation of clothing worn by human subjects. Ergonomics 26, 963–974.

Wissler, E.H., 2018. Human Temperature Control: A quantitative Approach, 1st ed. Springer, Berlin, Germany.

Xu, J., Psikuta, A., Li, J., Annaheim, S., Rossi, R.M., 2021. A numerical investigation of the influence of wind on convective heat transfer from the human body in a ventilated room. Build Environ 188, 107427.

Xu, J., Psikuta, A., Li, J., Annaheim, S., Rossi, R.M., 2019. Influence of human body geometry, posture and the surrounding environment on body heat loss based on a validated numerical model. Build Environ 166, 106340.

Ye, X.W., Xi, P.S., Su, Y.H., 2017. Analysis of non-stationary wind characteristics at an arch bridge using structural health monitoring data. J Civ Struct Health Monit 7, 573–587.

Yu, Y., Liu, J., Chauhan, K., de Dear, R., Niu, J., 2020. Experimental study on convective heat transfer coefficients for the human body exposed to turbulent wind conditions. Build Environ 169, 106533.

Zhou, S., Niu, J., 2022. Measurement of the convective heat transfer coefficient of the human body in the lift-up design, in: E3S Web of Conferences. EDP Sciences, p. 03001.

Zhou, S., Yu, Y., Niu, J., 2022. Field Measurement of the Human Body Convective Heat Transfer Outdoors. Available at SSRN 4283460.

Zou, J., Liu, J., Niu, J., Yu, Y., Lei, C., 2020. Convective heat loss from computational thermal manikin subject to outdoor wind environments. Build Environ 107469.

Zou, J., Yu, Y., Liu, J., Niu, J., Chauhan, K., Lei, C., 2021. Field measurement of the urban pedestrian level wind turbulence. Build Environ 194, 107713.

.